Wake dynamics of a square cylinder while moving upward in quiescent water

Intesaaf Ashraf,[a] Stephane Dorbolo,[a] and Neetu Tiwari[b]

(*Electronic mail: intesaaf.ashraf@ucl.ac.uk)

(Dated: 22 December 2025)

We experimentally investigate the water exit of a horizontally oriented square cylinder pulled vertically through a quiescent fluid at various Froude numbers (Fr). High-speed Particle Image Velocimetry (PIV) captures the velocity fields, from which we derive pressure distributions, swirl strength (λ_{ci})), shear-vortex interaction parameters (Λ), and the Okubo–Weiss scalar (W). Our analysis reveals the formation of a single, persistent clockwise (CW) and counterclockwise (CCW) vortex in the wake, with no signs of periodic vortex shedding. The swirl strength and Okubo–Weiss maps confirm an increasingly rotation-dominated flow at higher (Fr). Notably, the circulation exhibits a two-regime dependence on (Fr), mirroring the entrainment force behavior, whereas the vortex size itself remains nearly unchanged. These findings suggest that the intensified rotational motion, rather than an expanded vortex footprint, governs the enhanced entrainment and loading at high (Fr). Overall, the results provide new insights into the hydrodynamics of square cylinders in water-exit scenarios, highlighting the fundamental differences from classical cross-flow shedding and underscoring the pivotal influence of (Fr) on vortex strength and entrainment.

I. INTRODUCTION

The interaction of rigid bodies with free water surfaces during entry or exit processes is crucial across diverse engineering disciplines, such as naval architecture, ocean and coastal engineering, aviation, and dip-coating technologies. Due to the inherent complexities involving fluid-structure interactions, interfacial dynamics, and fluid mechanics, these phenomena remain challenging to interpret and accurately model.

Extensive research has explored the physics of bodies entering[1–4] and exiting fluids[5–8]. Recent studies have increasingly focused on water exit scenarios to deepen the understanding of associated flow dynamics, validate computational models, and guide the development of analytical frameworks[9–14].

Pioneering analytical work by Havelock [5] addressed the vertical motion of cylinders in uniform flow. Greenhow and Lin [15] subsequently performed experiments on a neutrally buoyant cylinder rising from a stationary position, observing characteristic bump-like free-surface deformations culminating in chaotic "waterfall breaking." Numerically, Telste [16] used potential flow theory to categorize the water exit of cylinders into three regimes: low-speed "wall-like" flow, intermediate-speed wave generation, and high-speed infinite-domain-like behavior. More recent experiments by Ashraf *et al.* [9] revealed symmetry-breaking wake instabilities in water in contrast to symmetric wakes in viscous silicone oil. They reported a two-stage drainage behavior of the entrained fluid, initially exponential, transitioning to a power-law decrease ($t^{-1/2}$) at later times, alongside a clear correlation of drag and entrainment forces with the Froude number.

Other researchers have also contributed significantly to the understanding of water exit processes. For instance, Greenhow and Moyo [17] performed two-dimensional simulations to investigate submerged cylinders in forced upward motion. Liju, Machane, and Cartellier [18] analyzed the surface surge phenomenon for cylinders of varying geometries and Reynolds numbers, while Moshari, Nikseresht, and Mehryar [19] employed Volume of Fluid (VOF) simulations to capture wave formation and air entrainment during oblique water exits. Additional numerical studies utilizing advanced VOF techniques were conducted by Kleefsman, Veldman, and Bunnik [20] and Nair and Bhattacharyya [21]. Experimental work by Chu *et al.* [22] identified cavity formation at cylinder extremities, resulting in water slapping upon cavity collapse during both accelerating and decelerating motions. In the context of spherical bodies, numerical analyses by Haohao *et al.* [8], employing Lattice Boltzmann methods (LBM), demonstrated a strong dependency of water-surface elevation on the Froude number, notably identifying intensified waterfall breaking at higher velocities. Furthermore, Ni, Zhang, and Wu. [23] observed delayed free-surface detachment for blunter spheroids. Experimentally, Truscott, Epps, and Munns [6] underscored the significance of the Reynolds number in determining vortex shedding and trajectories of buoyant spheres rising toward the surface, with distinct linear or oscillatory pathways based on initial depth. Complementary findings by Wu *et al.* [7] showed velocity-dependent surface elevations for fully submerged spheres, contrasting sharply with distinct columnar water detachments for partially submerged cases. Recently, comparative experimental analyses demonstrated that spheres with surface dimples significantly reduce drag and entrainment force coefficients at higher Froude numbers, enhancing water-exit efficiency, though leaving cross-over forces largely unaffected[10].

Previous research by Ashraf and Dorbolo [11] on square cylinder exit dynamics identified correlations between acting forces and the Froude number. In this study, it was also shown that below Fr ≈ 0.91, the entrainment force F_e rises sharply, reflecting rapid vortex-induced fluid uptake. Beyond this threshold, F_e increases gradually, indicating diminishing

[a]PtYX, Département de Physique, Université de Liège, 4000 Liège, Belgium
[b]Mechanical & Aerospace Engineering, Indian Institute of Technology Hyderabad, Kandi, Sangareddy, Telangana, India

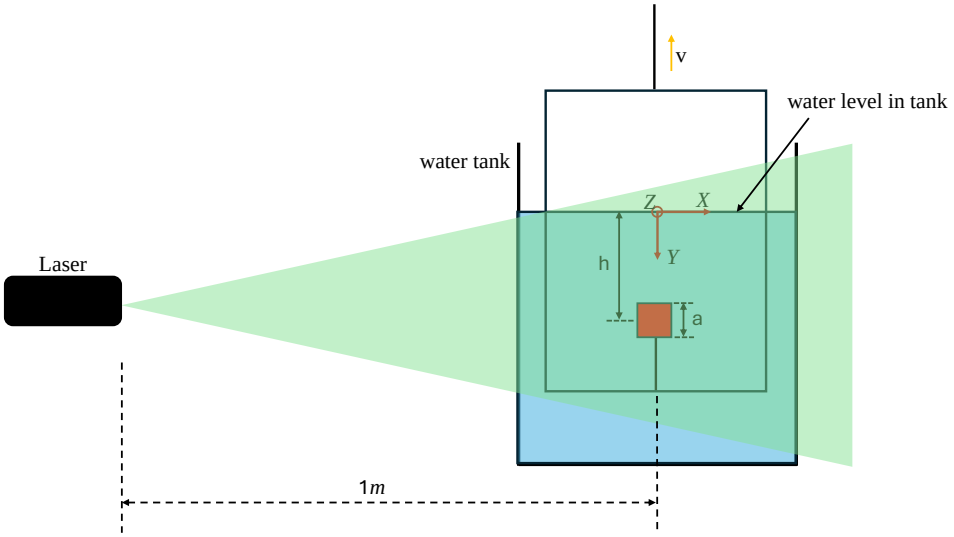

FIG. 1: The schematic of the PIV setup is illustrated, with the laser positioned 1 meter away from the cylinder's center. Image acquisition was performed at a frequency of 2000 Hz (figure is not to scale). See Ashraf and Dorbolo [11] for details.

returns in entrainment with further speed increments. However, it lacked a detailed explanation of the underlying flow-field mechanisms, especially these two different entrainment force regimes. The current study seeks to address this gap, specifically elucidating the mechanisms underlying the observed two-regime entrainment force behavior by examining wake dynamics during cylinder ascent.

II. METHODOLOGY

A. Experimental Set–up

The experimental setup comprised a lifting mechanism, a glass water tank (dimensions: 78.5 cm × 27.5 cm × 72.5 cm), PIV, and the test object. The lifting mechanism utilized a rack-and-pinion system, with the rack's moving part connected to a carbon fiber frame. This frame securely held the test cylinder in a horizontal orientation, parallel to the water tank's side and front walls. The test object was a right square cylinder, 3D-printed with square bases of side $a = 40\,\text{mm}$ and rectangular faces with a height $h = 220\,\text{mm}$. The cylinder was aligned horizontally to ensure that its square bases remained perpendicular to the water surface at all times. The experimental set-up has been explained in detail in the previous work of authors[11].

The 2D planar Particle Image Velocimetry (PIV) technique was employed for flow measurements. A laser with a 532 nm wavelength and 4 W peak power illuminated tracer particles of approximately 20 μm in diameter. Images were recorded at 2000 fps (frames per second) with an interrogation window size of 32×32 pixels, a magnification factor of 6.075 pixels/mm, and a field of view measuring $0.128\,\text{m} \times 0.205\,\text{m}$. The laser plane was aligned with the xy-plane at a distance of 1 m from the cylinder's center. The experimental setup for PIV measurements is depicted in Fig. 1. The acquired PIV images were post-processed using the open-source software PIVLab[24]. The coordinate system (XYZ) used in the experiment is shown in Fig. 1. The X-axis runs along the length of the tank, the Z-axis along its width, and the Y-axis represents the vertical direction, aligned with the pulling motion. The origin is set at the intersection between the pulling axis and the free water surface, defined as the horizontal plane (XZ). All coordinates were normalized by dividing them by a, the side length of the cylinder's square bases.

The experiments were performed at constant terminal velocities of 0.2 m/s, 0.25 m/s, 0.3 m/s, 0.4 m/s, 0.6 m/s, 0.8 m/s and 1 m/s, with a fixed acceleration of $4\,\text{m/s}^2$. To reach the fixed terminal velocity, the cylinder has to travel a predetermined distance from rest, such as 120 mm to achieve 1 m/s. The same conditions applied during the deceleration phase. The motion of the cylinder was verified to maintain constant speed during the PIV measurements.

B. Pressure Field Estimation from PIV

Two methods have generally been used for pressure estimation from PIV-measured velocity data. One of them is solving the Navier–Stokes equations via path integration[25]; the other is solving the pressure Poisson equation[26,27]. The pressure can be estimated from the Navier–Stokes equations as follows:

$$\nabla p = -\rho \frac{D\mathbf{u}}{Dt} + \mu \nabla^2 \mathbf{u} \tag{1}$$

where $\mathbf{u}$ is the fluid flow velocity, p is the pressure, ρ is the density, and μ is the local dynamic viscosity. The PIV-measured velocity data provide the information necessary to estimate the pressure gradient. In the Eulerian approach[28], the material (or total) acceleration can be expressed as

$$\frac{D\mathbf{u}}{Dt} = \frac{\partial \mathbf{u}}{\partial t} + (\mathbf{u} \cdot \nabla)\mathbf{u}. \tag{2}$$

There is a significant effect of the time separation between two consecutive snapshots on the accuracy of the estimated pressure field. For example, if we discretize the local acceleration term using a second-order finite difference scheme, we can define the associated truncation error as below:

$$\frac{\partial \mathbf{u}}{\partial t} = \frac{\mathbf{u}(x, t+\Delta t) - \mathbf{u}(x, t-\Delta t)}{2\Delta \mathbf{t}} + \frac{\Delta t^2}{6} \frac{\partial^3 \mathbf{u}}{\partial t^3} \tag{3}$$

where higher-order terms contributing to truncation error, $\frac{(\Delta t^2)}{6} \frac{\partial^3 \mathbf{u}}{\partial t^3}$, are usually neglected. The velocity measurement from PIV usually has uncertainty, so we measure velocity in the range $\mathbf{u} \pm \varepsilon_{\mathbf{u}}$, and the details of these uncertainty sources can be found in the literature[29]. Generally, uncertainties propagate when derivative terms of velocity are evaluated. In the local acceleration term, precision errors arise due to the velocity measurement uncertainty (ε_u))[30]:

$$\varepsilon^2 \frac{\partial u}{\partial t} \approx \frac{\sqrt{\varepsilon_{\mathbf{u}}^2 + \varepsilon_{\mathbf{u}}^2}}{4\Delta \mathbf{t}^2} \approx \frac{\varepsilon_{\mathbf{u}}^2}{2\Delta \mathbf{t}^2} \tag{4}$$

The effect of time separation on the truncation and precision errors is discussed in detail in the literature[30]. With a high sampling rate, time separation can be reduced, and the truncation error can also be reduced. However, precision errors will increase ([30]). Therefore, the pressure field estimated using the Navier-Stokes equations is not error-free, even with time-resolved data. Thus, for unsteady flows, the Poisson pressure equation is preferred; however, appropriate boundary conditions are critical. The Poisson pressure equation can be derived by taking the divergence of equation 1,

$$\nabla^2 p = -\rho \nabla . (\mathbf{u} . \nabla)\mathbf{u} \tag{5}$$

In this study, Dirichlet boundary conditions were selected. The pressure Poisson equation approach requires the evaluation of a second derivative of the velocity, which is not a direct measurement of PIV. The primary sources of error in the pressure Poisson equation are non-exact boundary conditions and the calculation of velocity gradients. However, by adopting specific measures during the experiments, the error can be minimized in the pressure Poisson equation ([31]). In the present study, in solving the pressure Poisson equation, the iteration was repeated until the root mean square error was reduced to the order of 10^{-5}.

C. Okubo–Weiss Parameter

To distinguish regions of shear-dominated flow from those dominated by rotation (vorticity), the Okubo–Weiss parameter (W)[32,33] is employed. For a two-dimensional, incompressible velocity field ($\mathbf{u} = (U, V)$), the parameter W is defined as:

$$W = s_n^2 + s_s^2 - \omega^2, \tag{6}$$

where

$$\omega = \frac{\partial V}{\partial x} - \frac{\partial U}{\partial y} \tag{7}$$

is the out-of-plane vorticity, and s_n, s_s are the normal and shear strain rates respectively. These strain rates are computed from the velocity-gradient tensor,

$$\nabla \mathbf{u} = \begin{bmatrix} \partial U/\partial x & \partial U/\partial y \\ \partial V/\partial x & \partial V/\partial y \end{bmatrix}, \tag{8}$$

by decomposing it into symmetric (strain) and antisymmetric (rotation) parts:

$$\nabla \mathbf{u} = \underbrace{\frac{1}{2}(\nabla \mathbf{u} + (\nabla \mathbf{u})^T)}_{\text{strain part}} + \underbrace{\frac{1}{2}(\nabla \mathbf{u} - (\nabla \mathbf{u})^T)}_{\text{rotation part}} \tag{9}$$

Specifically, the normal strain rate s_n and the shear strain rate s_s can be obtained from the eigenvalues or direct components of the symmetric part of $\nabla \mathbf{u}$.

Regions of flow where ($W < 0$) indicate rotation-dominated (elliptic) zones, typically identifying vortex cores. Conversely, $W > 0$ signifies shear-dominated (hyperbolic) zones, often surrounding the periphery of vortical structures. The computation of W is performed at each spatial grid point of the velocity field obtained via Particle Image Velocimetry (PIV). The resulting scalar field enables a clear delineation of coherent vortical regions and associated shear layers, providing additional insights beyond the raw vorticity field alone.

For numerical implementation, spatial gradients of $(\mathbf{u}, \mathbf{v})$ are calculated using a central-difference scheme. The vorticity (ω), normal strain (S_n), and shear strain (S_s) are then used in equation 6. This procedure yields instantaneous two-dimensional maps of (W), which can be time-averaged or analyzed on a frame-by-frame basis to characterize the flow topology in the wake of the moving cylinder.

D. Shear-Vortex Interaction Parameter

To analyze flow dynamics, first, the velocity gradient tensor (∇u) is computed by taking spatial derivatives of the velocity components as shown in equation 8

Then, swirl strength is computed as the imaginary part of the eigenvalues of the velocity gradient tensor. The eigenvalues (λ) of ∇U are obtained by solving:

$$\lambda = \frac{\mathrm{Tr}(\nabla \mathbf{u})}{2} \pm \sqrt{\left(\frac{\mathrm{Tr}(\nabla \mathbf{u})}{2}\right)^2 - \det(\nabla \mathbf{u})} \tag{10}$$

where:

$$\mathrm{Tr}(\nabla \mathbf{u}) = \frac{\partial \mathbf{u}}{\partial x} + \frac{\partial \mathbf{v}}{\partial y} (\text{trace of the matrix}) \tag{11}$$

$$\det(\nabla U) = \frac{\partial \mathbf{u}}{\partial x}\frac{\partial \mathbf{v}}{\partial y} - \frac{\partial \mathbf{u}}{\partial y}\frac{\partial \mathbf{v}}{\partial x} (\text{determinant}) \tag{12}$$

Swirl strength is then defined as:

$$\lambda_{ci} = \mathrm{Im}(\lambda) \tag{13}$$

where a higher λ_{ci} indicates stronger local rotational intensity.

Vorticity is another key measure of rotational motion in the flow. Unlike swirl strength, which isolates vortex cores, vorticity accounts for both rotational and shear-dominated regions. Then, a dynamic thresholding method is applied to separate vortex cores from shear regions. The threshold is based on a fraction (α) of the maximum swirl strength in the flow:

$$\lambda_{ci,\text{threshold}} = \alpha \cdot \lambda_{ci,\max} \tag{14}$$

where $\alpha = 0.05$ in this analysis. Regions where:

$$\lambda_{ci} > \lambda_{ci,\text{threshold}} \tag{15}$$

are classified as vortex cores, while regions where λ_{ci} is below the threshold are classified as shear-dominated regions. Finally, to quantify the interaction between shear and vortex structures, the Shear-Vortex Interaction Parameter Λ is computed as:

$$\Lambda = \frac{\int_{\text{shear}} dA}{\int_{\text{vortex}} dA} \tag{16}$$

where:

- $\int_{\text{shear}} dA$ is the integral of the areas classified as shear regions.
- $\int_{\text{vortex}} dA$ is the integral of the areas classified as vortex regions.

A value of $\Lambda > 1$ indicates shear-dominated flow, whereas $\Lambda < 1$ suggests vortex dominance.

E. Vortex Dynamics Charaterization

To analyze the vortical structures in the wake of a square cylinder, we employed a methodology based on detecting coherent vortex regions using the *swirl strength* (λ_{ci}) and vorticity (ω)[34–36]. The dataset, obtained through Particle Image Velocimetry (PIV), contains velocity field information at discrete time steps. The primary steps involved in the vortex identification process are as follows:

Preprocessing: The velocity components $(\mathbf{u}, \mathbf{v})$ were smoothed using a Gaussian filter to reduce noise and ensure stable vortex detection.

Velocity Gradient Computation: The velocity field was numerically differentiated to obtain the velocity gradient tensor using the equation 8.

Swirl Strength Calculation: The swirl strength is calculated as defined in equation 13.

Vorticity Calculation: The vorticity field was also computed using the equation 7.

A combination of swirl strength and vorticity magnitude was used to differentiate shear layers from vortex cores[37].

Morphological Processing: To ensure spatial continuity of vortex regions, morphological closing was applied using a disk structuring element.

Vortex Region Labeling and Filtering: Connected vortex regions were identified using an 8-connectivity labeling algorithm. Only the largest clockwise (CW) and counterclockwise (CCW) vortex per frame were retained to remove spurious detections.

Circulation and Vortex Size Computation: The circulation (Γ) and vortex area (A) for the largest vortex were computed as:

$$\Gamma = \sum_{\text{vortex region}} \omega \, dx \, dy, \tag{17}$$

$$A = \sum_{\text{vortex region}} dx \, dy. \tag{18}$$

The detected vortex regions were visualized using a color-mapped vorticity field, where red and blue contours corresponded to the largest detected CW and CCW vortices, respectively.

III. RESULTS AND DISCUSSION

A. Overall Flow Evolution and Pressure Distribution

Figures 2 illustrate the flow structures and pressure distributions around the square cylinder at different Froude numbers (Fr). The wake remains characterized by a single, stable counterclockwise (CCW) vortex without evidence of periodic vortex shedding. The pressure field analysis confirms the persistence of a low-pressure zone behind the cylinder, whose size and intensity grow with increasing (Fr).

For low Froude numbers $(\mathrm{Fr} < 0.3)$, the wake features a small, confined negative-pressure region at the cylinder's trailing edge, indicating a weak recirculation zone. The surface deformation is minimal, and only a thin water layer is carried upward.

For moderate Froude numbers $(0.3 \leq \mathrm{Fr} \leq 1.0)$, the wake expands, with the CCW vortex intensifying. The surface deformation becomes more significant, leading to enhanced entrainment of fluid.

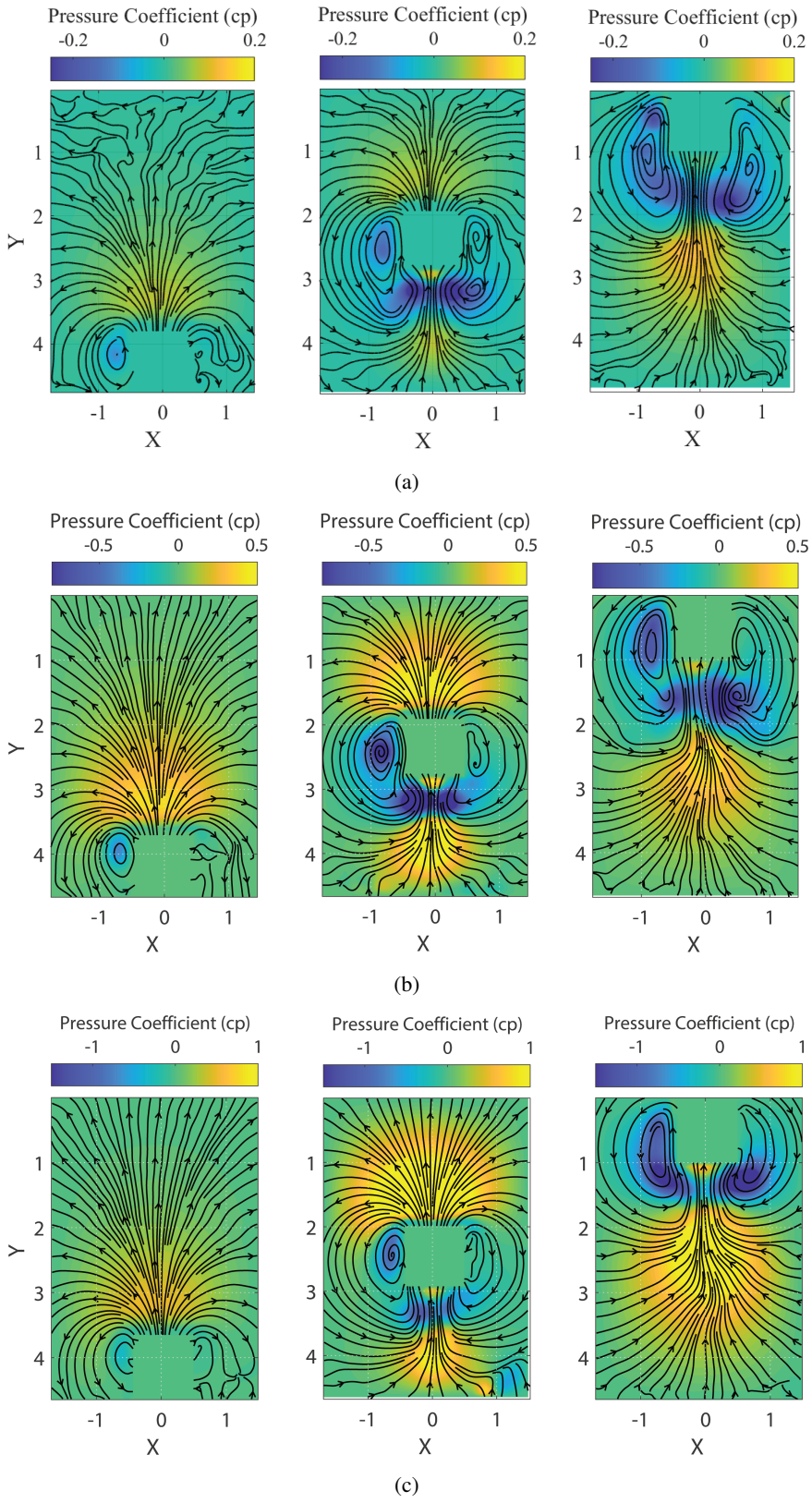

FIG. 2: Flow structure during the exit of a square cylinder at Froude number, (a) Fr = 0.16, (b) Fr = 0.90, and (c) Fr = 2.54.

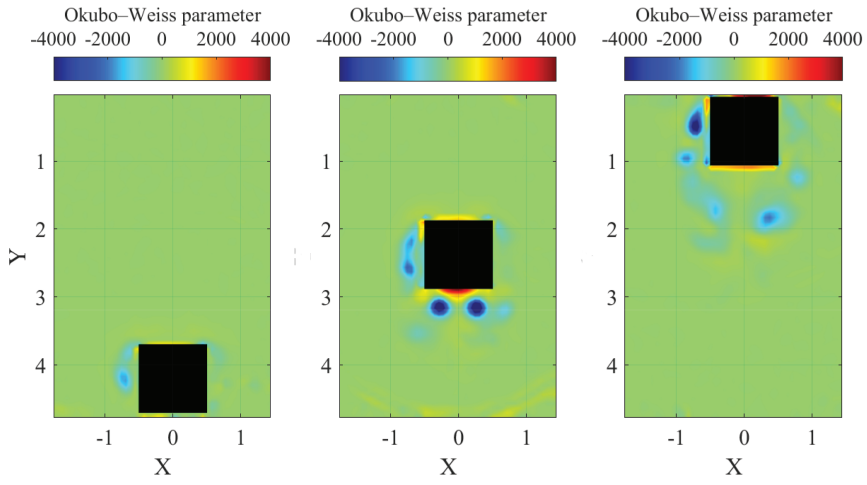

(a)

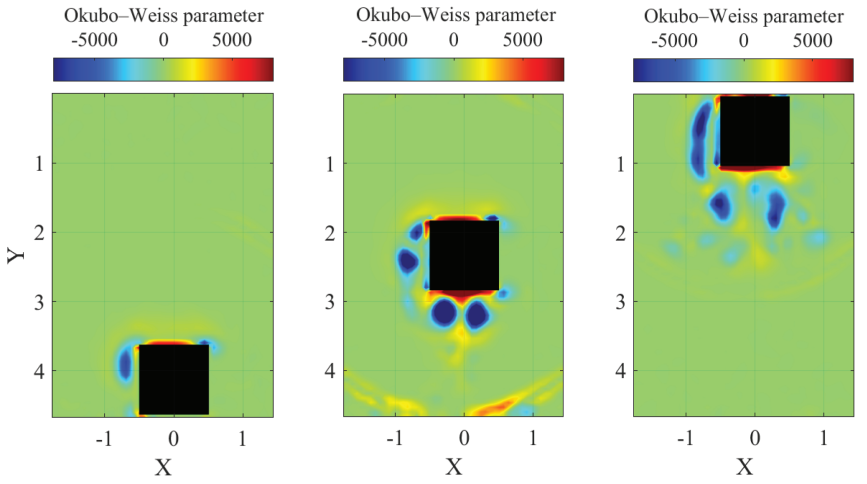

(b)

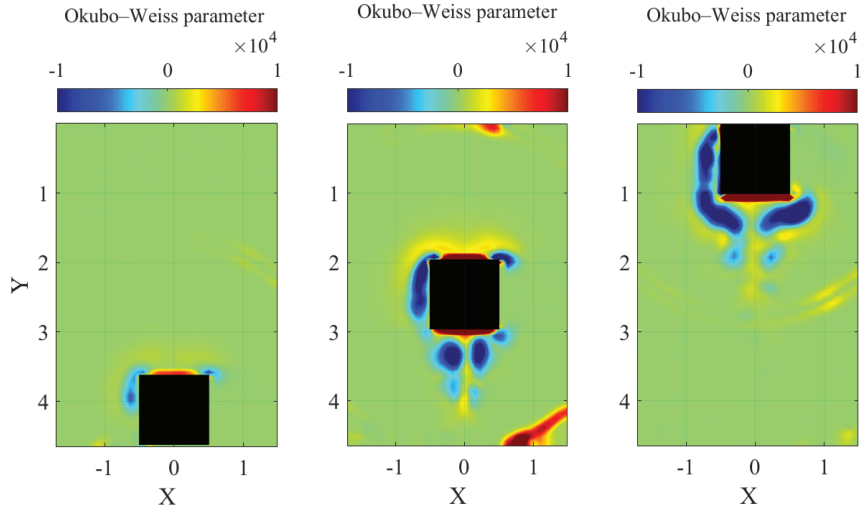

(c)

FIG. 3: Okubo–Weiss parameter (W) during the exit of a square cylinder at (a) Froude number, Fr = 0.16, (b) Fr = 0.90, and (c) Fr = 2.54.

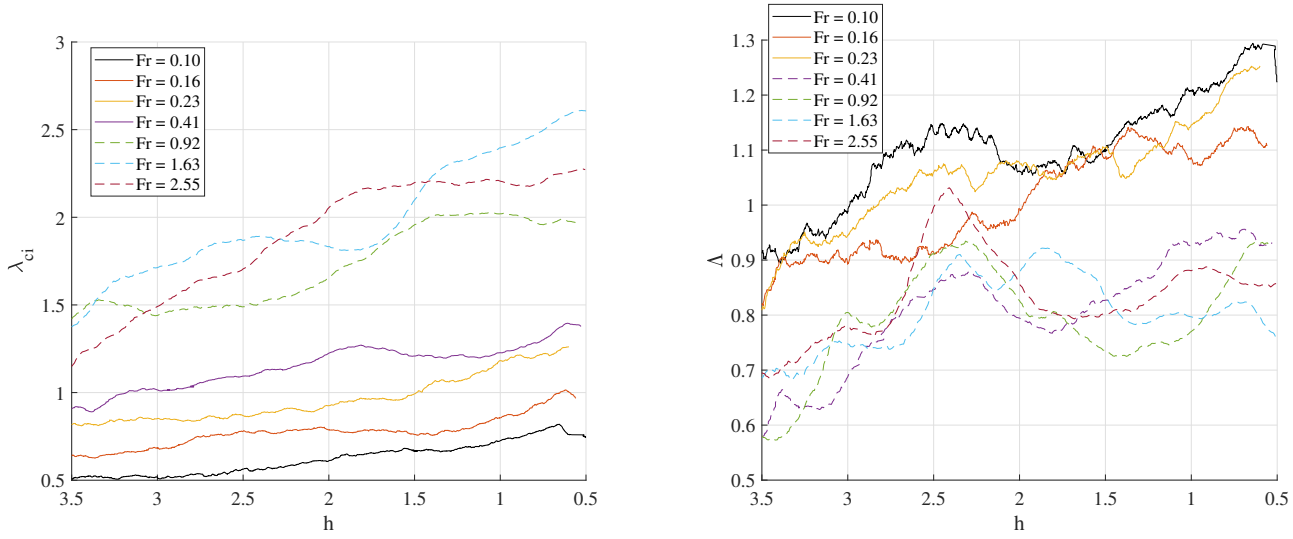

(a) (b)

FIG. 4: (a) Mean swirl strength (λ_{ci}) as a function of the dimensionless submergence depth (h) for different Froude numbers (Fr). Higher (Fr) values generally produce larger (λ_{ci}), indicating a more intense vortex. The increase in (λ_{ci}) near ($h \approx 0.5$) suggests stronger rotational motion as the cylinder approaches the free surface. (b) Shear-vortex interaction parameter (Λ) versus the dimensionless submergence depth (h) for various Froude numbers. The peaks observed at intermediate (h) for higher (Fr) indicate stronger interaction between shear layers and vortex cores, whereas lower (Fr) values exhibit relatively modest variations in (Λ). As (h to 0.5), (Λ) decreases, reflecting the dominance of rotational (vortex-dominated) regions near the free surface.

For high Froude numbers (Fr > 1.0), the negative-pressure zone behind the cylinder enlarges significantly, corresponding to a more intense vortex. High pressures emerge near the cylinder's top surface due to stagnation and vertical fluid displacement. Despite this stronger wake, no alternating vortex shedding occurs.

B. Okubo–Weiss Parameter Analysis

To distinguish between rotation-dominated and shear-dominated regions, we analyze the Okubo–Weiss parameter (W) (Figures 3). The results confirm that the wake is consistently rotation-dominated, reinforcing the absence of vortex shedding. At low (Fr), there is a small, localized negative-(W) region behind the cylinder, with weak shear layers. As (Fr) increases to moderate and high values, the negative-(W) region expands significantly, mirroring the growth of the low-pressure wake. No transition to shedding is observed.

C. Swirl Strength, Shear-Vortex Interaction, and Correlation with Okubo–Weiss Parameter

Figures 4(a) and 4(b) depict the mean swirl strength (λ_{ci}) and the shear-vortex interaction parameter (Λ) as functions of the dimensionless submergence depth (h) for various Froude numbers (Fr). These quantities complement the insights gained from the Okubo–Weiss parameter (W), which differentiates rotation-dominated ($W < 0$) from shear-dominated ($W > 0$) regions.

As (h) decreases toward 0.5 (i.e., the cylinder nears the free surface), (λ_{ci}) generally increases, indicating a progressive intensification of the vortex.

Higher (Fr) fosters stronger swirl at nearly every depth, consistent with the expansion of negative-(W) zones seen in the Okubo–Weiss maps. Specifically, large negative-(W) regions align with high swirl strengths, underscoring the enhanced rotational motion at elevated speeds.

This behavior aligns with the two-regime trend observed in both the Okubo–Weiss analysis and circulation/entrainment data, wherein flows transition around (Fr ≈ 1.0) to a more vigorous rotational state.

The plots show that, at moderate to high (Fr), (Λ) can exhibit a local maximum around ($h \approx 2$), suggesting a depth where shear layers interact robustly with the vortex core before the flow fully transitions near the free surface.

For lower (Fr), (Λ) remains comparatively stable, indicating minimal shear–vortex coupling in agreement with a smaller region of negative (W). In other words, there is less separation between shear and rotation-dominated regions at low speeds.

The Okubo–Weiss parameter (W) provides a global distinction between rotation- and shear-dominated zones; the swirl strength (λ_{ci}) and the shear-vortex interaction parameter (Λ) offer finer detail about how strong rotational motion is (via λ_{ci}) and how shear layers compete with vortex cores (via Λ).

Large negative-(W) regions coincide with high Λ, reflect-

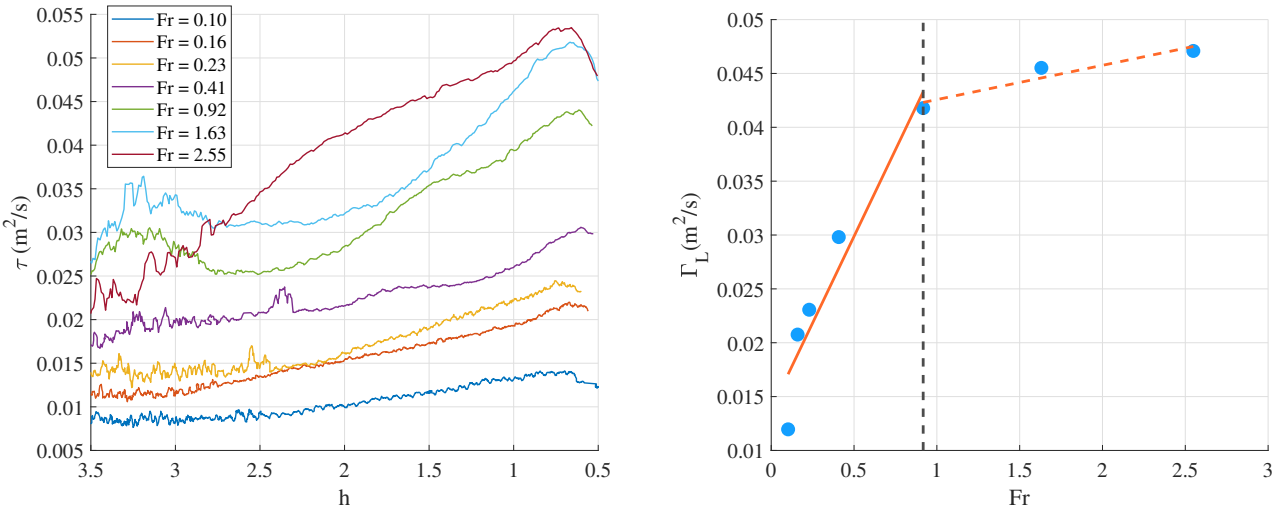

FIG. 5: (a) Circulation (τ) of counter clockwise (CCW) vortex as afunction of the cylinder's position h at different Froude number. (b) The circulation of anti-clockwise (CCW) vortex at $h = 0.5$ at different Froude numbers.

ing robust vortex-dominated areas. Significant shear-vortex interplay (peaks in Λ) appears where (W) may shift from positive to negative values, capturing the interface between shear-dominated (positive (W)) and rotation-dominated (negative (W)) zones.

Overall, the swirl strength and shear-vortex interaction analyses reinforce the Okubo–Weiss observations, painting a consistent picture of how vortex intensity (λ_{ci}) and shear versus rotation balance (Λ and W) evolve with submergence depth and Froude number. These correlated findings underline the key role of vortex-dominated regions in determining the exit dynamics of the square cylinder, especially as (Fr) increases.

D. Vortex Circulation and Area

We quantify the vortex strength by analyzing the circulation of counter clockwise (CCW) vortex (τ) (Figures 5(a)) as function of the position of the cylinder, h and the circulation (Γ_L) of the counter clockwise vortex (CCW) at $h = 0.5$ just when the cylinder reaches the free water surface and cylinder starts coming out of water after that. In addition, we also plot the vortex area (A) of the CCW vortex as a function of h (Figures 6).

The circulation increases as the cylinder approaches the free surface ($h \approx 0.5$), then stabilizes or slightly decreases due to surface interactions. The circulation of counter clockwise (CCW)(Γ_L) at $h = 0.5$ exhibits a two-regime behavior: a steep rise below (Fr ≈ 1.0), followed by a shallower increase beyond this threshold.

However, unlike circulation, the vortex area, although it appears to vary during motion, looks relatively independent of the Froude number, (Fr) values. This suggests that while the rotational intensity of the vortex increases with (Fr), its physical size is largely independent.

E. Maximum Circulation and Similarity to Entrainment Force

Figure 5(b) shows that the maximum circulation at $h = 0.5$ follows a trend similar to the entrainment force reported in prior studies Ashraf and Dorbolo [11]. This suggests a fundamental link between the wake vortex and the fluid mass carried above the free surface.

1. **Low- to moderate-Fr regime (Fr < 1.0):** Circulation and entrainment force rise rapidly as stronger vortices entrain increasing amounts of fluid.

2. **High-Fr regime (Fr > 1.0):** While both circulation and entrainment force continue to increase, the slope decreases. This suggests a saturation effect, where further speed increments yield diminishing vortex growth.

IV. CONCLUSIONS

In this paper, we have experimentally studied the exit dynamics of a square cylinder rising through quiescent water at different Froude numbers (Fr). Time-resolved Particle Image Velocimetry (PIV) data enabled us to reconstruct velocity fields, compute pressure distributions, and perform vortex characterization using swirl strength (λ_{ci}), shear-vortex interaction (Λ), and the Okubo–Weiss parameter (W).

1. **Persistent CCW and CW Vortex and Absence of Shedding:** Despite the cylinder's high velocity at large (Fr, no von Kármán-type shedding patterns emerge. Instead, a single counterclockwise and clockwise vortex remains attached to the cylinder throughout its upward path.

2. **Two-Regime Behavior in Circulation and Entrainment:** The circulation of the CCW vortex grows rapidly

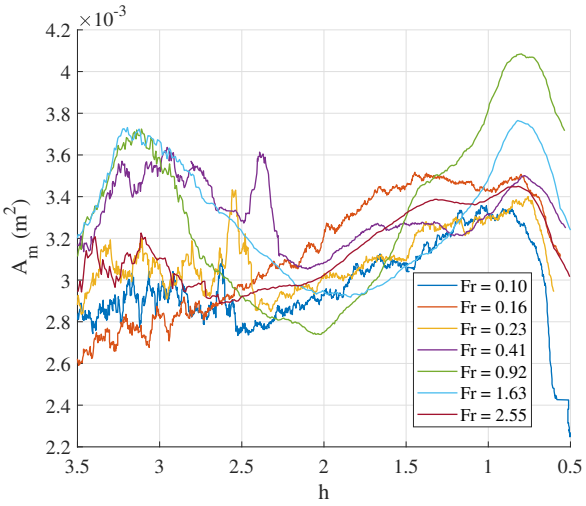

FIG. 6: Area of counter clockwise (CCW) vortex was a function of h at different Froude numbers.

for ($\mathrm{Fr} < 1.0$), then more gradually beyond that threshold. This correlates closely with the entrainment force measured in previous studies Ashraf and Dorbolo [11], indicating a flow transition near ($\mathrm{Fr} \approx 1.0$).

3. **Swirl Strength Increases While Vortex Area Remains Constant:** Both swirl strength (λ_{ci}) and negative-(W) regions expand at higher Fr, reflecting stronger rotational motion. The physical size of the vortex remains changes but the behavior seems independent of the Froude number Fr. It implies that an enhanced vortex intensity, rather than an enlarged vortex footprint, drives the larger entrainment.

4. **Shear-Vortex Interaction Peaks at Intermediate Depths:** The shear-vortex interaction parameter (Λ) tends to attain a local maximum at $h \approx 2$ for higher Fr, signifying robust shear-layer and vortex-core interplay before the cylinder intersects the free surface.

5. **Dominance of Rotational Flow Near the Surface:** As the cylinder nears $h = 0.5$, Λ decreases, indicating diminished shear layers and stronger vortex-driven motion. Swirl strength also spikes in this zone, underscoring the wake's transition to a primarily rotation-dominated state.

In conclusion, the upward translation of a square cylinder in a quiescent fluid creates an evolving wake dominated by a single CCW and CW vortex whose intensity increases with Fr. This intensified rotation, rather than a broader vortex core, fosters higher entrainment forces at large Fr. The flow thus exhibits distinct two-regime behavior, separated around $\mathrm{Fr} \approx 1.0$, and differs markedly from classical cross-flow shedding processes. Our findings are relevant for designing surface-piercing and exit maneuvers of naval and offshore structures, where understanding vortex dynamics and entrainment forces is critical for reliable performance and safety.

ACKNOWLEDGMENTS

The financial support of the Belgian Fund for Scientific Research under research project WOLFLOW (F.R.S.-FNRS, PDR T.0021.18) is gratefully acknowledged. Part of the experimental setup was financed by *Fonds Spéciaux* from ULiège. SD is F.R.S–FNRS Senior Research Associate

AUTHOR CONTRIBUTIONS

DATA AVAILABILITY

The Data can be made available upon reasonable request to the authors.

REFERENCES

[1] R. Challa, S. C. Yim, V. G. Idichandy, and C. P. Vendhan, "Rigid-object water-entry impact dynamics: Finite-element/smoothed particle hydrodynamics modeling and experimental validation," Journal of Offshore Mechanics and Arctic Engineering **136**, 3 (2014).

[2] R. Challa, V. G. Idichandy, C. P. Vendhan, and S. Yim, "An experimental study on rigid-object water-entry impact and contact dynamics," in *ASME 2010 29th International Conference on Ocean, Offshore and Arctic Engineering* (American Society of Mechanical Engineers Digital Collection, 2010) pp. 383–391.

[3] A. Mohtat, R. Challa, S. C. Yim, and C. Q. Judge, "Numerical modeling of hydrodynamic impact and local slamming effects," in *SNAME International Conference on Fast Sea Transportation* (SNAME, 2015) p. D031S011R003.

[4] Q. Yang and W. Qiu, "Numerical simulation of water impact for 2d and 3d bodies," Ocean Engineering **43**, 82–89 (2012).

[5] T. H. Havelock, *The forces on a circular cylinder submerged in a uniform stream* (Proceedings of the royal society A, 1936).

[6] T. T. Truscott, B. P. Epps, and R. H. Munns, "Water exit dynamics of buoyant spheres," Physical Review Fluids **1**, 7 (2016).

[7]Q. G. Wu, B. Y. Ni, X. L. Bai, B. Cui, and S. L. Sun, "Experimental study on large deformation of free surface during water exit of a sphere," Ocean Engineering **140**, 369–376 (2017).
[8]H. Haohao, S. Yanping, Y. Jianyang, C. Fu, and L. Tian, "Numerical analysis of water exit for a sphere with constant velocity using the lattice boltzmann method," Applied Ocean Research **84**, 163–178 (2019).
[9]I. Ashraf, L. Vincent, R. Falla, V. E. Terrapon, B. Scheid, and S. Dorbolo, "Experimental investigation of the exit dynamics of a horizontal circular cylinder out of water and silicone oil," Physical Review Fluids **9**, 124005 (2024).
[10]I. Ashraf and S. Dorbolo, "Effect of the surface dimples on the exit dynamics of a sphere at a constant velocity," Applied Ocean Research **147**, 103996 (2024).
[11]I. Ashraf and S. Dorbolo, "Exit dynamics of a square cylinder," Ocean Engineering **297**, 117106 (2024).
[12]K. Takamure, T. Uchiyama, and T. Degawa, "Motion characteristics of sphere with uniaxial through-hole after passing through air–water interface: Case study with different submergence depths," Applied Ocean Research **154**, 104341 (2025).
[13]X. Huang, Y. Dai, and X. Zhu, "Numerical study of vehicle motion during water exit under combined lifting force and wave action," Physics of Fluids **36** (2024).
[14]B. Zhou, Z. Zhao, Q. Dai, W. Yao, X. Liu, Y. Zhang, A. Wang, and H. Zhang, "Numerical study on the cavity dynamics of water entry and exit for a high-speed projectile crossing a wave," Physics of Fluids **36** (2024).
[15]M. Greenhow and W.-M. Lin, "Nonlinear-free surface effects: experiments and theory," (1983), technical report, Massachusetts Inst Of Tech Cambridge Dept Of Ocean Engineering.
[16]J. Telste, "G,"inviscid flow about a cylinder rising to a free surface,"," in *Journal of Fluid Mechanics, Vol. 182* (1987) pp. 149–168.
[17]M. Greenhow and W. Moyo, Simiso, "entry and exit of horizontal circular cylinders,"," Philosophical Transactions of the Royal Society of London. Series A: Mathematical, Physical and Engineering Sciences **355**, 551–563 (1997).
[18]P. Y. Liju, R. Machane, and A. Cartellier, "Surge effect during the water exit of an axisymmetric body traveling normal to a plane interface: experiments and bem simulation," Experiments in fluids **31**, 241–248 (2001).
[19]S. Moshari, A. H. Nikseresht, and N. Mehryar, Reza, "analysis of two and three dimensional buoyancy driven water-exit of a circular cylinder,"," International Journal of Naval Architecture and Ocean Engineering **6**, 219–235 (2014).
[20]K. M. T. Kleefsman, A. E. P. Veldman, and T. Bunnik, *An improved {V} olume of {F} luid i {VOF} method for wave impact type problems* (Proceedings of OMAE-FPSO, 2004).
[21]V. V. Nair and S. K. Bhattacharyya, "Water entry and exit of axisymmetric bodies by cfd approach," Journal of Ocean Engineering and Science **3**, 156–174 (2018).
[22]X.-S. Chu, K. Yan, Z. Wang, K. Zhang, G. Feng, and W. qi Chen, "Numerical simulation of water-exit of a cylinder with cavities," Journal of Hydrodynamics, Ser. B **22**, 877–881 (2010).
[23]B. Y. Ni, A. M. Zhang, and G. X. Wu., "Simulation of complete water exit of a fully-submerged body," Journal of Fluids and Structures **58**, 79–98 (2015).
[24]W. Thielicke and E. Stamhuis, "Pivlab–towards user-friendly, affordable and accurate digital particle image velocimetry in matlab," Journal of open research software **2** (2014).
[25]N. Tiwari, Y. Tasaka, and Y. Murai, "Pressure field estimation from ultrasound doppler velocity profiler for vortex-shedding flows," Flow Measurement and Instrumentation **67**, 23–32 (2019).
[26]N. Tiwari and Y. Murai, "Ultrasonic velocity profiler applied to explore viscosity–pressure fields and their coupling in inelastic shear-thinning vortex streets," Experiments in Fluids **62**, 185 (2021).
[27]N. Tiwari, Y. Tasaka, and Y. Murai, "Piv-based estimation of viscosity and pressure fields for a steady pseudoplastic flow," Flow Measurement and Instrumentation **77**, 101852 (2021).
[28]J. Van der Kindere, A. Laskari, B. Ganapathisubramani, and R. de Kat, "Pressure from 2d snapshot piv," Experiments in Fluids **60**, 32 (2019).
[29]A. Sciacchitano, "Uncertainty quantification in particle image velocimetry: A topical review," Measurement Science and Technology **30** (2019), 10.1088/1361-6501/ab1db8.
[30]B. van Oudheusden, "Piv-based pressure measurement," Measurement Science and Technology **24**, 032001 (2013).
[31]C. Pan, J. Xiong, M. Wang, Q. Feng, and X. Cui, "Pressure field reconstruction from particle image velocimetry velocity field by the omnidirectional virtual boundary integration method," Experiments in Fluids **57**, 1–16 (2016).
[32]A. Okubo, "Horizontal dispersion of floatable particles in the vicinity of velocity singularities such as convergences," in *Deep sea research and oceanographic abstracts*, Vol. 17 (Elsevier, 1970) pp. 445–454.
[33]J. Weiss, "The dynamics of enstrophy transfer in two-dimensional hydrodynamics," Physica D: Nonlinear Phenomena **48**, 273–294 (1991).
[34]H. Chen, Z. Wang, L. Zhu, and J. Wang, "Evaluation of vortex identification methods based on two-and three-dimensional swirling strengths," Physics of Fluids **30** (2018).
[35]Q. Chen, Q. Zhong, X. Wang, and D. Li, "An improved swirling-strength criterion for identifying spanwise vortices in wall turbulence," Journal of Turbulence **15**, 71–87 (2014).
[36]B. Morton, "The strength of vortex and swirling core flows," Journal of Fluid Mechanics **38**, 315–333 (1969).
[37]P. Chakraborty, S. Balachandar, and R. J. Adrian, "Kinematics of local vortex identification criteria," Journal of visualization **10**, 137–140 (2007).

V. APPENDIXES

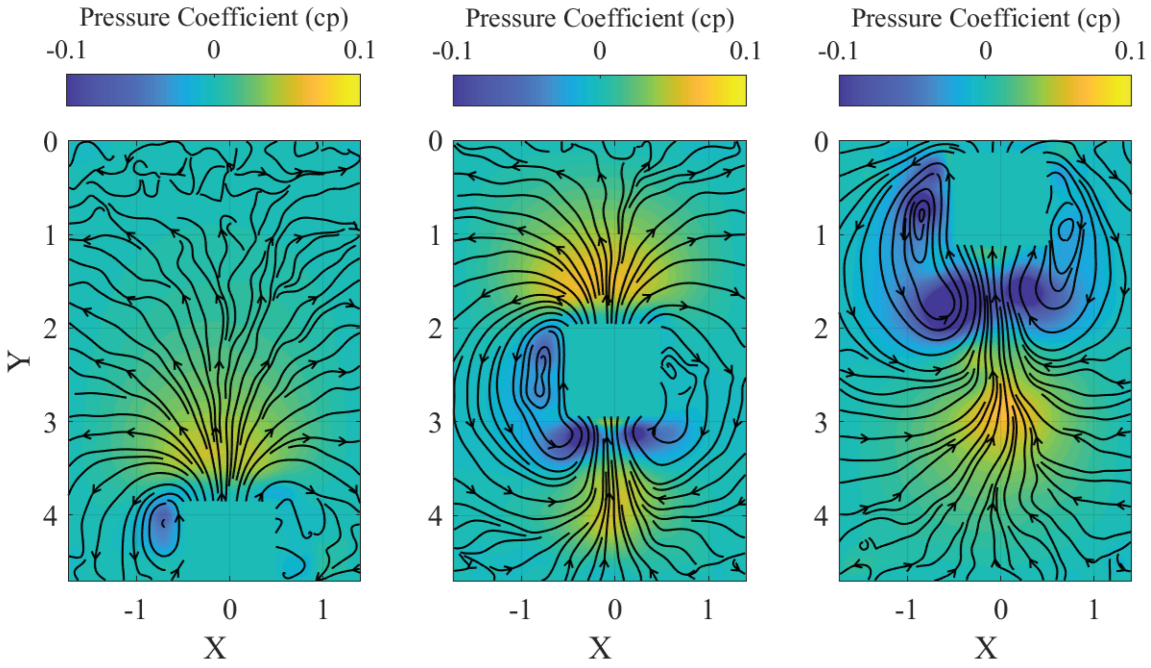

FIG. 7: Flow structure during the exit of a square cylinder at Froude number, Fr= 0.10.

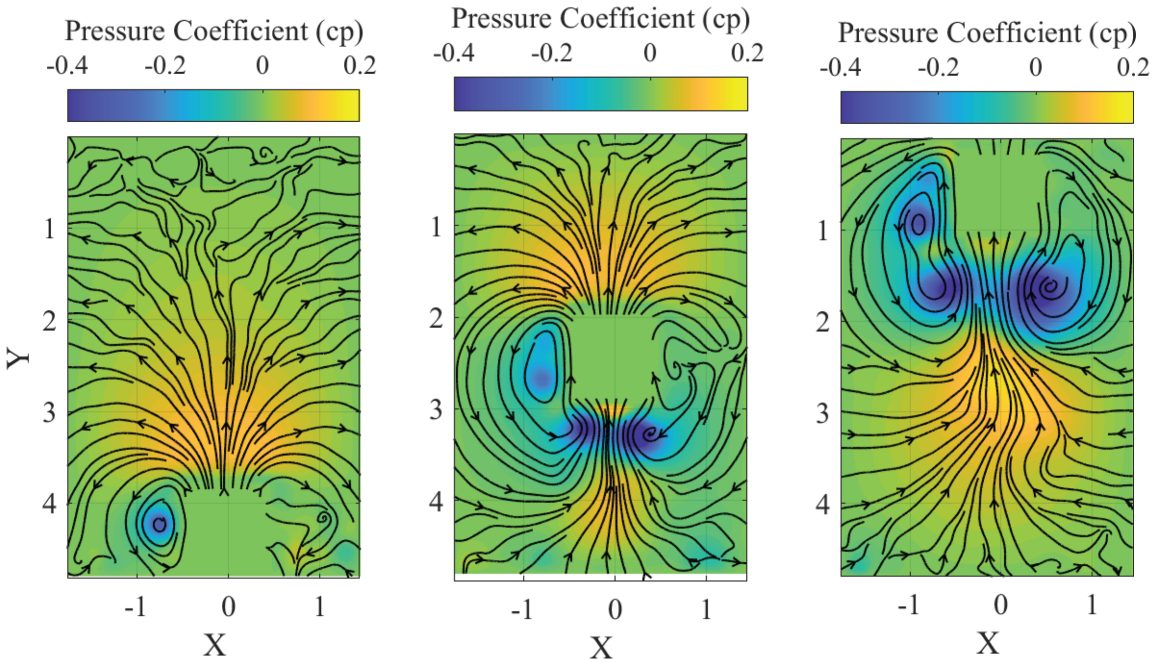

FIG. 8: Flow structure during the exit of a square cylinder at Froude number, Fr= 0.23

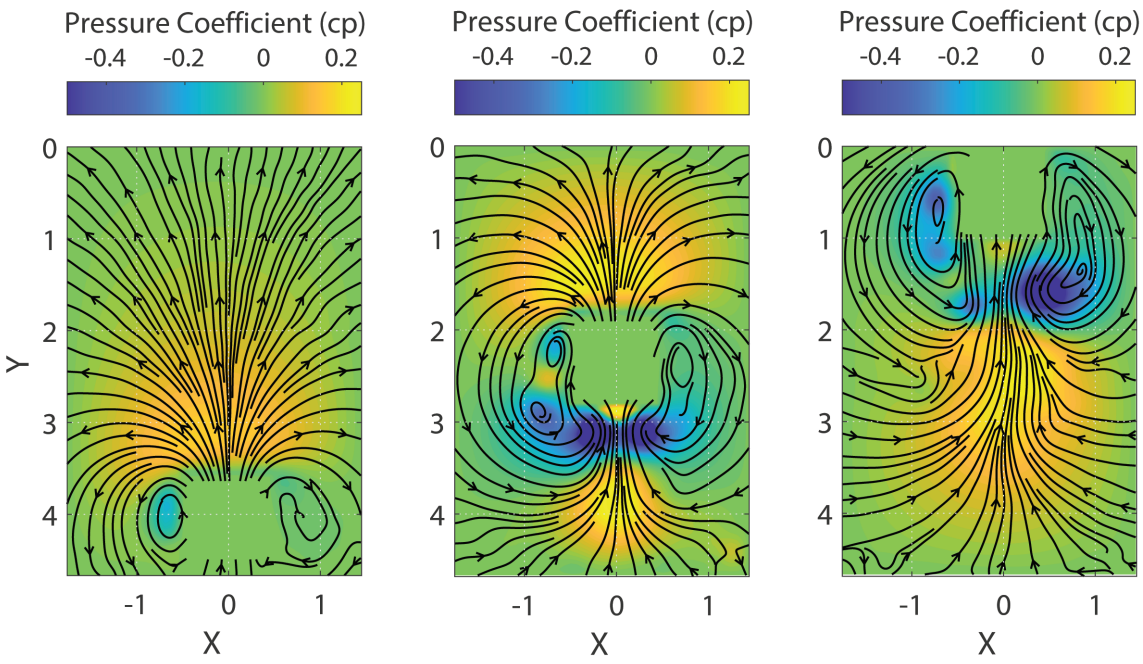

FIG. 9: Flow structure during the exit of a square cylinder at Froude number, Fr= 0.40

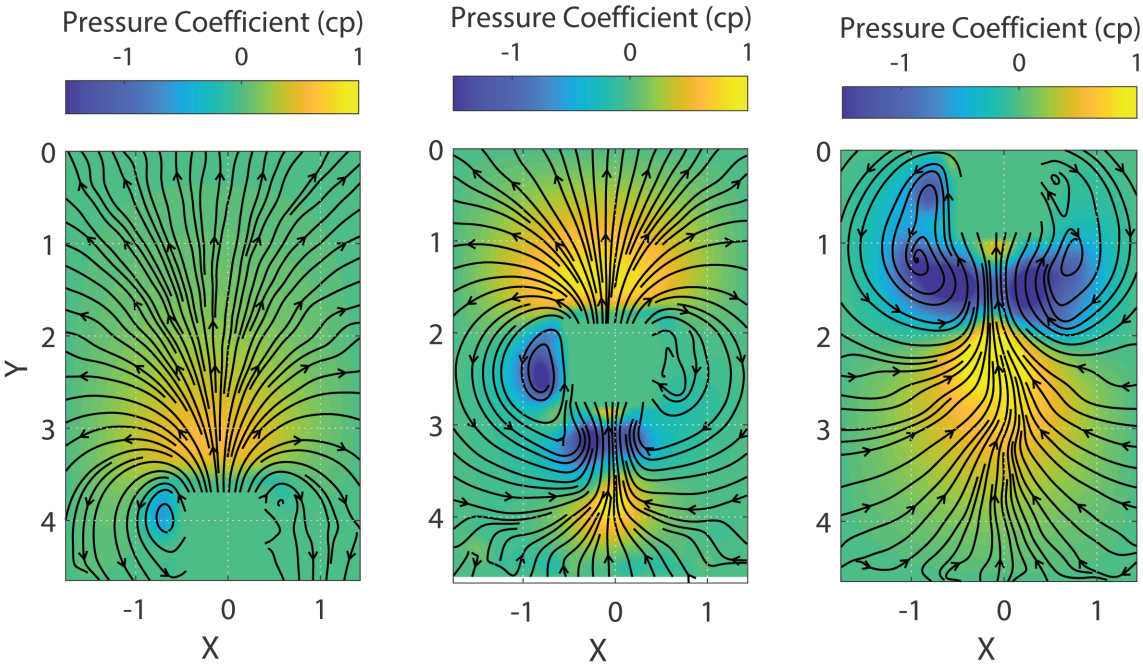

FIG. 10: Flow structure during the exit of a square cylinder at Froude number, Fr = 1.61

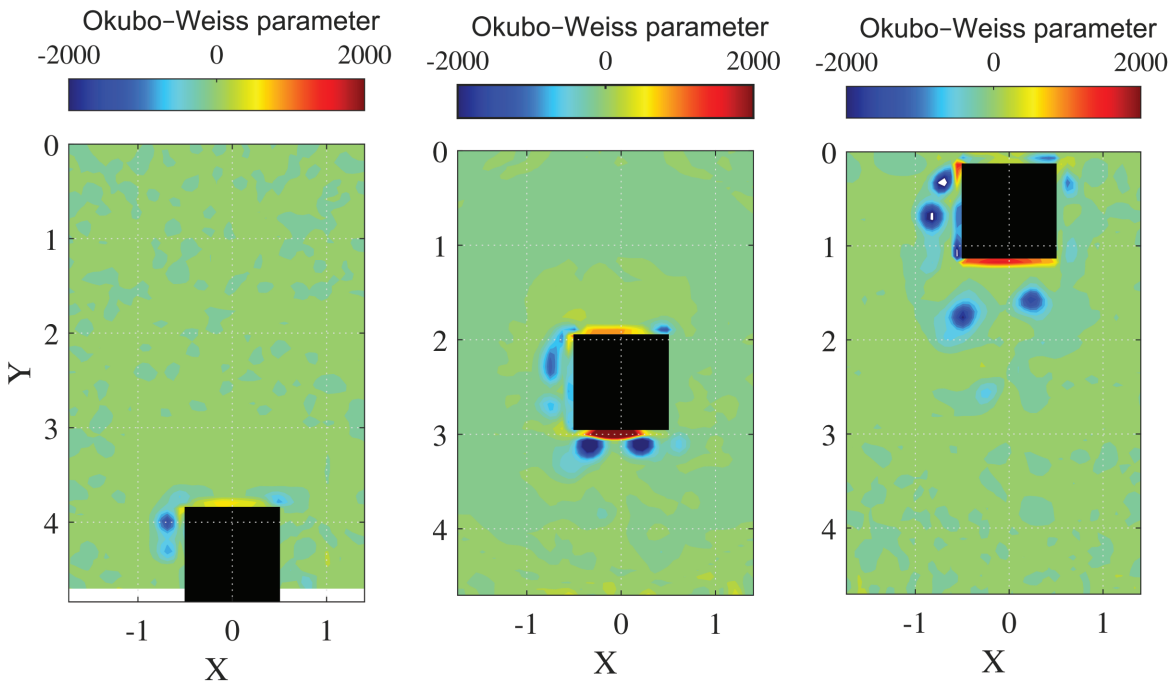

FIG. 11: Okubo–Weiss parameter (W) during the exit of a square cylinder at Froude number, Fr= 0.10.

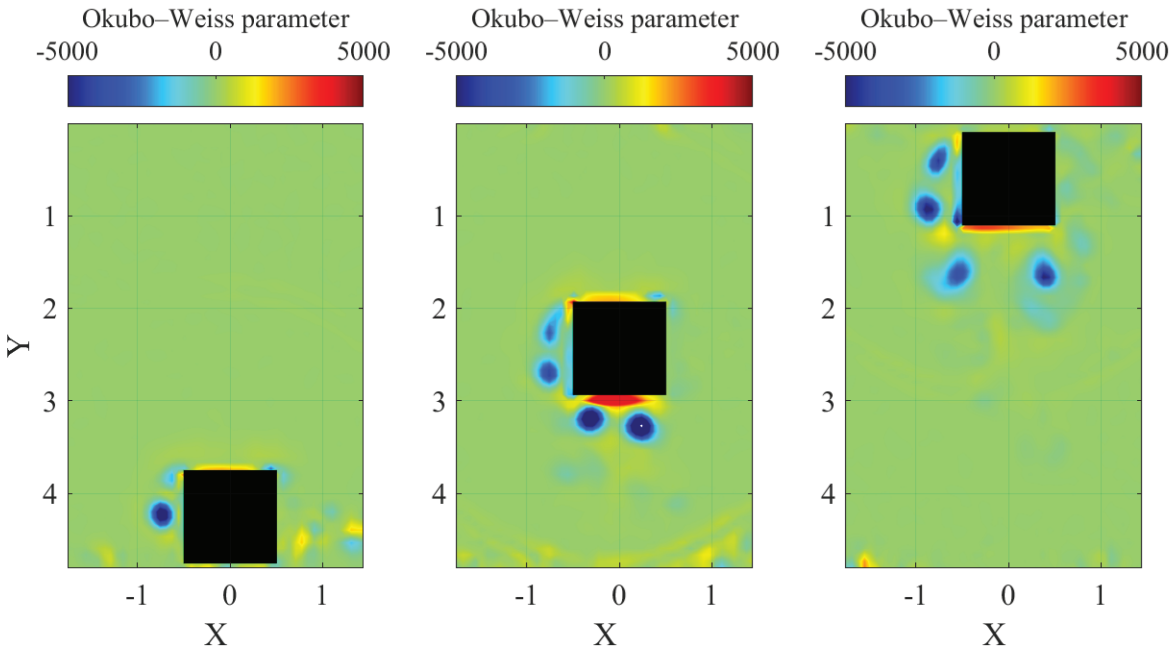

FIG. 12: Okubo–Weiss parameter (W) during the exit of a square cylinder at Froude number, Fr= 0.23

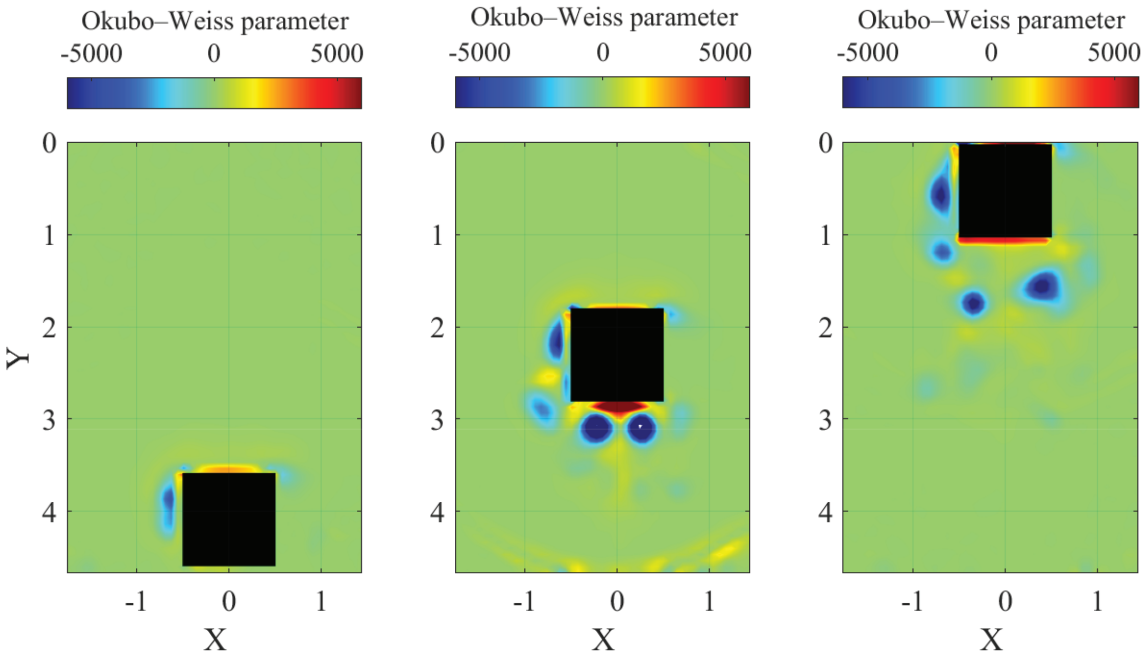

FIG. 13: Okubo–Weiss parameter (W) during the exit of a square cylinder at Froude number, Fr= 0.40

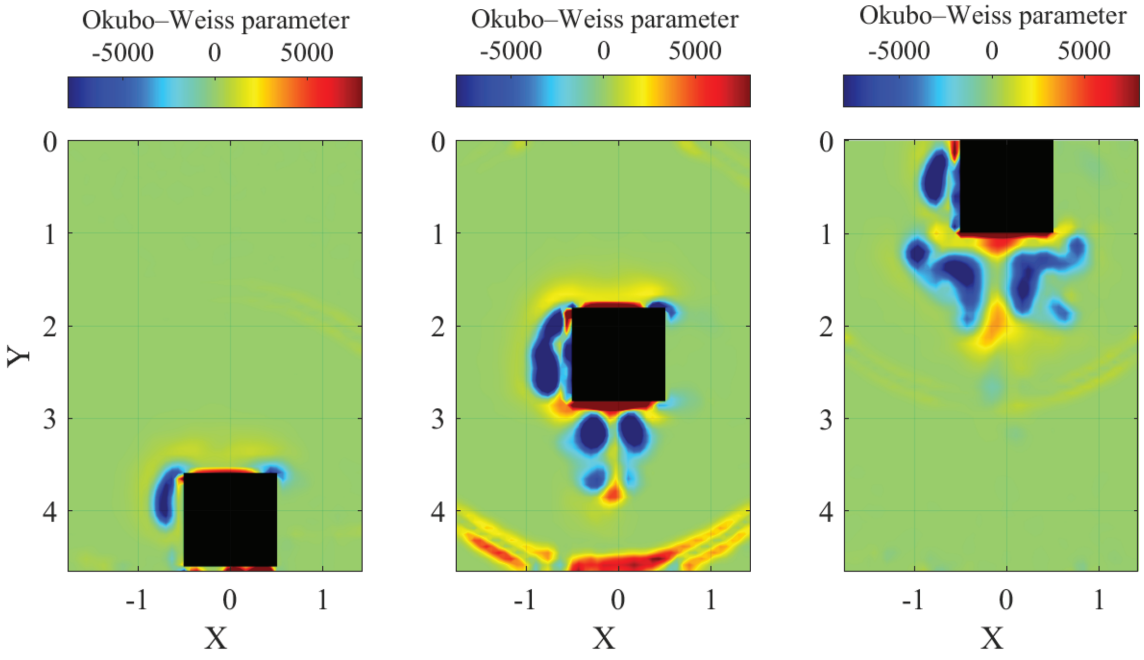

FIG. 14: Okubo–Weiss parameter (W) during the exit of a square cylinder at Froude number, Fr = 1.61